Broadband and widely tunable second-harmonic generation in suspended thin-film LiNbO3 rib waveguides

Aiman Zinaoui, Lucas Grosjean, Arthur de Sousa Lopes Moreira, Miguel Angel Suarez, Samuel Queste, Laurent Robert, Ludovic Gauthier-Manuel, Mathieu Chauvet, Nadège Courjal

APL Photonics LETTER pubs.aip.org/aip/app

Broadband and widely tunable second harmonic generation in suspended thin-film $LiNbO_3$ rib waveguides

Cite as: APL Photon. 9, 000000 (2024); doi: 10.1063/5.0230481
Submitted: 24 July 2024 • Accepted: 2 October 2024 •
Published Online: 9 99 9999

View Online Export Citation CrossMark

Aiman Zinaoui, Lucas Grosjean, Arthur De Sousa Lopes Moreira, Miguel Angel Suarez, Samuel Queste, Laurent Robert, Ludovic Gauthier-Manuel, Mathieu Chauvet, and Nadège Courjal[a]

AFFILIATIONS

FEMTO-ST Institute, UMR CNRS 6174, University of Franche-Comte, 15B Avenue des Montboucons, 25000 Besancon, France

[a]Author to whom correspondence should be addressed: nadege.courjal@femto-st.fr

ABSTRACT

Our study demonstrates second harmonic generation (SHG) in a high confinement $LiNbO_3$ rib waveguide through type-I birefringence phase matching of fundamental modes. The combination of micro-waveguide dispersion and material birefringence reveals unique SHG characteristics that complement the performance of standard $LiNbO_3$ on insulator components. Dual-pump wavelength phase matching in the near-infrared and mid-infrared regions is shown in a given waveguide. These two wavelengths can be positioned in the 1.1–3.5 μm range or converge near 1.5 μm by adjusting the core waveguide size or through temperature tuning. A 25 °C temperature change enables a broad pump tunability band of 300 nm, ranging from 1350 to 1650 nm, with a conversion efficiency exceeding 40%/(W/cm^2) within a single waveguide. A temperature tuning range of up to 900 nm is foreseen by tailoring the waveguide core size. In addition, a broadband response of 150 nm within the telecom window is demonstrated experimentally. The nonlinear waveguide, etched in a thin film membrane, is combined with titanium-indiffused waveguides to form a monolithic $LiNbO_3$ component. This configuration provides low coupling losses of 0.8 dB and single-mode operation. It paves the way for a new generation of versatile and cost-effective frequency conversion components with wide-band spectral responses suitable for optical communications, environmental sensing, and quantum information processing.

I. INTRODUCTION

Quadratic phase-matched nonlinear processes for frequency conversion are pivotal in both quantum and classical optics, with significant potential for emerging applications, such as photonic spiking neurons,[1] broadband spectroscopy,[2] high-brightness single-photon sources,[3] and quantum frequency converters.[4] However, a larger deployment of these applications faces challenges in achieving broad spectral operation, high nonlinear conversion efficiency, and fiber-compatible integration within a single component. Periodically poled lithium niobate on insulator (PPLNOI) structures, which ensure quasi-phase-matching (QPM) in sub-micrometer cross-section $LiNbO_3$ on insulator (LNOI) waveguides, are promising due to their record-breaking nonlinear conversion efficiencies[5] of 2600%/(W/cm^2) benefiting from a high nonlinear coefficient ($d_{33} = d_{zzz} = 27$ pm/V)[6] and tight light confinement. Their ability to operate at any wavelengths within the material transparency range (0.35–5 μm)[7–9] is also widely appreciated. Nevertheless, the converted bandwidth remains constrained to a few nanometers near the targeted wavelength due to strict phase matching conditions. Broader bandwidth of up to 110 nm has been demonstrated by varying the poling period through step-chirp,[10] but this approach significantly degrades the nonlinear conversion efficiency to 9.6%/(W/cm^2). Tailoring the waveguide dispersion can yield broad operational bandwidths while maintaining high conversion efficiencies. This has been demonstrated at mid-infrared wavelengths,[11,12] with bandwidths and nonlinear conversion efficiencies of 110 nm and 1100%/(W/cm^2), respectively.

However, PPLNOI fabrication tolerances are restrictive[13] and also suffer from low in-coupling efficiencies. Micrometer-thick $LiNbO_3$ layers can improve fiber integration[14] and fabrication tolerances but at the expense of a compromise between

operational bandwidth and conversion efficiency. In addition, thermal tunability of the SHG response remains challenging in type-0 PPLNOI waveguides, with a thermal tuning rate typically below 0.5 nm/°C.

Intermodal phase matching is an alternative solution to periodic poling that requires adapting the waveguide geometry to reach perfect phase matching. Challenges of poor mode overlap have been addressed using antisymmetric waveguides by taking advantage of the phenomenon of bound states in the continuum[15] or through layer poling[16] with a type-0 configuration, achieving nonlinear conversion efficiencies of 300%/(W/cm^2) and 4615%/(W/cm^2), respectively. However, thermal tunability remains low, around 0.18 nm/°C.

By enabling perfect phase matching between two orthogonally polarized fundamental modes, birefringence phase matching (BPM) in micro-waveguides offers a poling-free approach that provides a large overlap and noncritical coupling between the SH and pump modes with lower coupling losses.[17] Another advantage of this method is its temperature tunability coefficient near 1 nm/°C.[18]

This study demonstrates an ultra-wide bandwidth second harmonic generation (SHG) response in a poling-free monolithic $LiNbO_3$ component using type-I birefringence phase matching. The SH signal is generated in a rib waveguide fabricated within an air-suspended $LiNbO_3$ membrane, which is coupled to tapers to give low-loss pigtailing with standard fibers.[19] Our experimental results show a conversion bandwidth exceeding 150 nm, covering the entire third telecom band, with a conversion efficiency of 40%/(W/cm^2). In addition, temperature tuning extends the conversion range from 1.35 to 1.65 μm, thus spanning the two main windows of the telecom band. These high-performance metrics are achieved by balancing material and waveguide dispersion, resulting in a tunable dual phase-matching condition between the transverse electric (TE_{00}) and transverse magnetic (TM_{00}) modes over a broad bandwidth.

II. THEORETICAL STUDY

The reported second harmonic generation (SHG) process achieves perfect phase matching by balancing the intrinsic birefringence of an $LiNbO_3$ crystal with a tailored dispersion in a nonlinear rib waveguide. This specific type-I phase matching between the fundamental modes of the TM_{00} pump and the TE_{00} SH is demonstrated with the monolithic $LiNbO_3$ component shown in Fig. 1, where the nonlinear process takes place in the air-suspended rib waveguide located in the central part.

This rib waveguide is adiabatically combined with two titanium-diffused waveguides at both the input and output sides through tapered sections, providing a gradual transition from a single-mode input waveguide with a cross section of ~30 μm^2 to the fundamental mode of the nonlinear area with a cross section of about 4 μm^2. The adiabatic transitions not only ensure optimal excitation of the fundamental mode with 0.8 dB/facet coupling losses[19] but also facilitate light injection and collection, thus enhancing the overall SHG efficiency.

The perfect type-I SHG phase-matching condition is fulfilled in the rib waveguide when

$$\Delta n = n_{pump} - n_{SH} = \frac{\lambda_{pump}\Delta k}{4\pi} = 0, \quad (1)$$

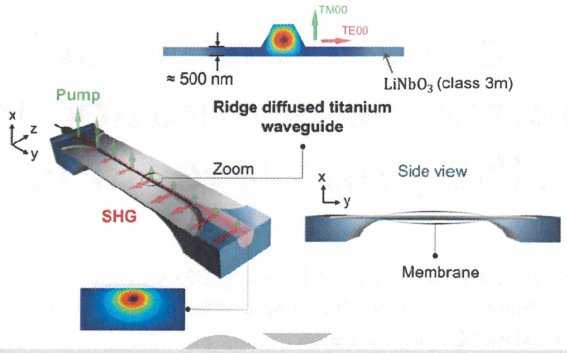

FIG. 1. Artistic view of a $LiNbO_3$ frequency doubling component constituted of a central nonlinear suspended membrane rib waveguide, with a highly confined mode, adiabatically coupled to large cross-section input and output titanium-diffused single-mode waveguides.

where n_{pump} and n_{SH} are the effective indices of the pump and SH modes, respectively, and Δk is the wave vector mismatch. Δn is dependent on the birefringence of $LiNbO_3$ and on the rib dimensions.

In our simulations, the material's refractive index is given by the Sellmeier equations[20,21] corrected for slight titanium doping. However, it should be noted that titanium doping has a negligible effect on the effective indices of the modes in the rib waveguide. Phase matching can be adjusted by choosing the geometry of the rib waveguide, which depends on the width, height, sidewall angle, and thickness, as shown in Fig. 2(a). The sidewall angle is set to 15° due to the manufacturing process. As first insight, simulations are performed for different waveguide cross sections [defined as mean width × (height + thickness), where the mean width is the average width of the cross section, including the sidewall angle] using COMSOL®. Figure 2(b) shows the phase mismatch Δn vs the pump wavelength for different rib waveguide cross sections at ambient temperature. For large waveguide cross sections, we notice that dual phase matching occurs at two distinct pump wavelengths, one near 1 μm in the near-infrared (NIR) and the other in the mid-infrared (MIR) near 3 μm, as in bulk crystals. As the waveguide cross section is decreased, these two phase-matched wavelengths become closer until they merge for a cross section of about 5 μm^2. Our study focuses on this latter waveguide configuration that displays near-phase-matched conditions for a wide range of telecom wavelengths. For cross sections smaller than 5 μm^2, phase matching vanishes.

It is essential to note that $LiNbO_3$ birefringence significantly depends on temperature. Indeed, the extraordinary index varies with temperature contrary to the ordinary index, which is almost temperature independent.[21,22] Consequently, temperature is an efficient parameter for adjusting the phase-matching condition. As an illustration, in Fig. 2(b), a rib waveguide with an 8 μm^2 cross section enables two phase-matched pump wavelengths separated by 500 nm at room temperature. As this waveguide is heated, the two wavelengths shift closer to each other and merge at 95 °C, as shown in Fig. 2(c), resulting in a broad phase-matching bandwidth around 1500 nm.

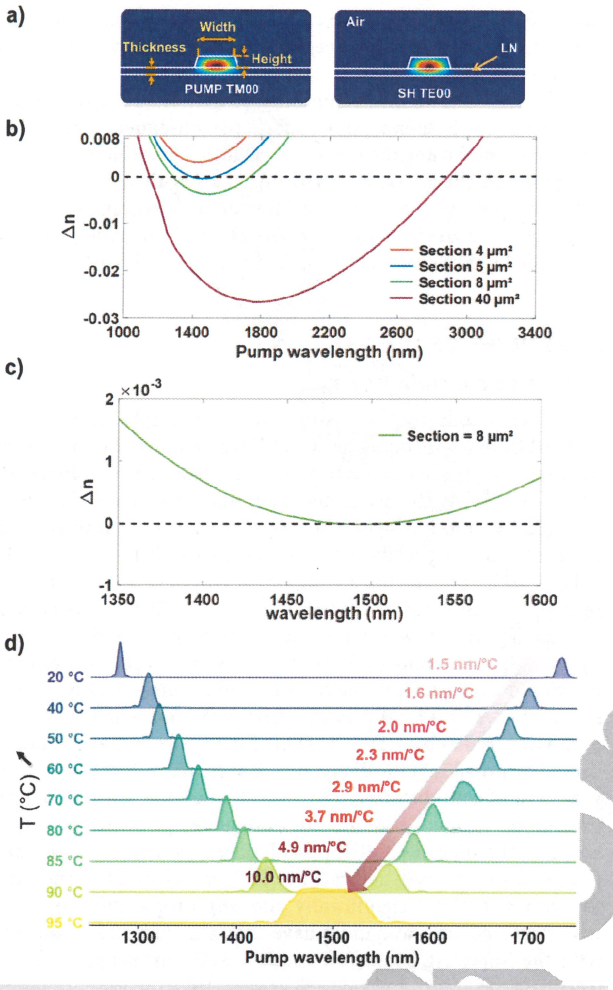

FIG. 2. Theoretical study of the SHG birefringent phase matching in a rib waveguide using a finite elements method (f.e.m.) of COMSOL software. (a) Rib waveguide geometry and fundamental mode distributions for the pump (1.55 μm) and the SH. (b) Calculation of the phase mismatching for four waveguide cross sections vs pump wavelength. (c) Phase mismatch in an 8 μm^2 cross-section waveguide (width = 3.8 μm, height = 1.2 μm and thickness = 800 nm) at 95 °C and (d) conversion efficiency vs temperature and wavelength in the same waveguide.

To evaluate the conversion efficiency η, the following equation is used:[18]

$$\eta = \frac{P_{SH}}{P_{pump}^2 L^2} = \frac{8\pi^2}{\varepsilon_o c n_{pump}^2 n_{shg} \lambda_{pump}^2} \frac{OI^2 d_{31}^2}{A_{eff}}, \quad (2)$$

where P_{SH} is the rib waveguide output power for the SH, P_{pump} is the rib waveguide input power for the pump, c is the speed of light in vacuum, ε_o is the dielectric permittivity of vacuum, d_{31} is the second-order nonlinear coefficient equal to 4.3 pm/V, which corresponds to the d_{zxx} element of the non-linear susceptibility tensor after its simplification using the group symmetry of $LiNbO_3$ class 3 m, A_{eff} is the effective mode area, OI is the spatial overlap integral of the two modes, and L is the length of the nonlinear interaction. Figure 2(d) shows the normalized conversion efficiency for an 8 μm^2 cross-section waveguide of length L = 1 mm as a function of wavelength and temperature in the non-depleted pump regime. It shows that with the chosen geometry (width = 3800 nm, height = 1230 nm, and thickness = 800 nm), the conversion efficiency is estimated to be 55%/(W/cm^2) with a weak dependence with wavelength. It also confirms that the two phase matched pump wavelengths can be tuned over a range of 500 nm by changing the temperature from 20 to 95 °C. At the phase-matching temperature of 95 °C, this waveguide exhibits a 100 nm ultra-broadband phase-matched SHG interaction, allowing high spectral acceptance for pump wavelengths in the telecom band. The giant thermal tuning range is a direct consequence of the unique dispersion profile of the waveguide. It should be noted that the thermal tuning rate ($\frac{\partial \lambda_{pump}}{\partial T}$) is highly nonlinear with the value changing from 1.5 nm/°C near room temperature (low-temperature dependence regime) to 10 nm/°C (strong-temperature dependence regime) when approaching broadband conversion [see the red data in Fig. 2(d)]. As the waveguide temperature increases, the refractive index mismatch for SHG, denoted as Δn, grows because the extraordinary index rises more significantly than the ordinary index.[21] This shift causes the phase-mismatch curves [see Fig. 2(b)] to move upward with increasing temperature. For waveguides with larger cross sections (e.g., the green curve), the two phase-matched wavelengths thus shift toward the telecom band. The rate of this shift is given by $\frac{\partial \lambda_{PM}}{\partial T} = \frac{\partial \lambda_{PM}}{\partial \Delta n} \frac{\partial \Delta n}{\partial T}$. While the second term of the equation is mainly given by the thermo-optical property of $LiNbO_3$, the first term is the inverse slopes of the curves shown in Fig. 2(b) at the phase-matched wavelengths λ_{PM}, which is proportional to the group velocity mismatch. This explains the nonlinear temperature tuning rate we observed, which increases from 1 to 10 nm/°C as the phase-matched wavelengths approach the telecom band, where the slope becomes minimal. Such a high tuning rate of 10 nm/°C is more than nine times higher than the best results reported in the literature,[23] enabling a wide tunability range. However, the trade-off of this high-temperature sensitivity regime is the need for increasingly precise and stable temperature control as the interaction length increases.

Changing the waveguide geometry provides a means to modify the pump tunability band and, to a lesser extent, the conversion efficiency. For instance, reducing the waveguide cross section to 6 μm^2 (width = 2700 nm, height = 1550 nm, and thickness = 500 nm) enhances the conversion efficiency to 60%/(W/cm^2). In addition, this modification allows a pump tunability band ranging from 1370 to 1550 nm, which can be achieved with a minimal temperature variation of 12 °C due to an average thermal tuning rate of 6 nm/°C (see Fig. 3). The conversion efficiency enhancement is linked to the lower A_{eff} value in Eq. (2). Conversely, increasing the waveguide cross section will lead to expanded tunability. A pump tunability of more than 900 nm is anticipated with a temperature variation of 200 °C in a 23 μm^2 cross-section waveguide. It is noteworthy that any selected pump wavelength in the 1–3.5 μm range can be phase-matched by properly dimensioning the waveguide.

To further analyze the influence of the waveguide geometry on the phase matching, we then set the pump wavelength to 1550 nm and vary the width and height of the waveguide

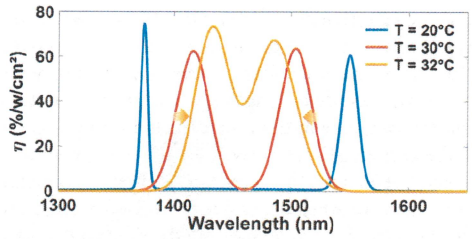

FIG. 3. Broadband response at room temperature using a rib waveguide with a cross section equal to 6 μm^2, which corresponds to a rib geometry of width = 2700 nm, height = 1550 nm, and thickness = 500 nm. This simulation is performed in the non-depleted pump regime.

initially considered in Fig. 3. Figure 4(a) shows that the increase in the rib waveguide height from 1.5 to 1.75 μm can be compensated by a decrease in the width from 3 to 2 μm to maintain a perfect phase matching. Two additional curves show the tolerance to perfect phase matching to maintain an SHG response better than half the optimum value. This latter condition is fulfilled when $|\Delta n| \leq \frac{0.4429\lambda}{2L}$, which leads to $|\Delta n| \leq 3 \times 10^{-4}$ refractive index unit (RIU) for L = 1 mm. Given this condition, the dimensional tolerance for the rib waveguide is 3 μm ± 65 nm in width or 1.5 μm ± 20 nm in height. It is, however, essential to note that reaching the phase-matching condition does not imply fabricating a waveguide with absolute dimensions. Indeed, the fabrication constraints can be relaxed since the operating temperature is a powerful adjustment tool. As an illustration, Fig. 4(b) shows the phase-matching condition as a function of temperature and rib height for a waveguide width of 2.7 μm. It shows that we can compensate for a 220 nm rib waveguide height offset by a temperature variation of 70 °C.

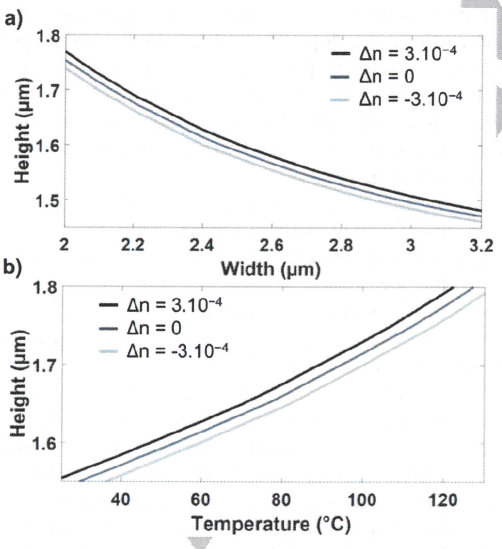

FIG. 4. Phase matching condition ($\Delta n = 0$) at a pump wavelength of 1550 nm and for a thickness of 500 nm as a function of the rib waveguide geometry at room temperature (a) and as a function of temperature and height (b) for a 2.7 μm wide waveguide. Tolerance to perfect phase matching for a 1 mm long waveguide is also displayed ($\Delta n = \pm 3 \times 10^{-4}$).

Figure 4 shows that a minimum height of ~1.4 μm is required to achieve the phase-matching condition. Consequently, the $LiNbO_3$ films fabricated using the ion-slicing technology, which usually have a submicron thickness, are inadequate for realizing the proposed SHG component. For the experimental demonstration, we chose to construct a device with a nonlinear rib waveguide based on a suspended membrane carved out of a monolithic $LiNbO_3$ wafer.

III. EXPERIMENTAL RESULTS

A. Device manufacturing

Using a collective fabrication process, multiple components are realized from a 4 in. diameter X-cut $LiNbO_3$ wafer. As schematically shown in Fig. 5, the process begins with manufacturing single-mode titanium-indiffused waveguides. Titanium strips are etched from a 90 nm thick titanium layer. The strips are 6 μm wide at their extremities, transitioning to the rib waveguide's width in the 1 mm long central SHG zone, giving a component length of 2 cm. Diffusion is realized at a temperature of 1045 °C for 8 h and 50 min. As a first step to realizing the rib waveguides, a nickel mask is used to form ribs by reactive ion etching (RIE) with horizontal transitions from the Ti indiffused waveguides to the central confined area. Finally, the backside of the wafer is locally diced below each central SHG zone with a precision circular saw (DISCO DAD 3350) to form the membrane. It should be noted that the dicing not only creates $LiNbO_3$ membranes with a uniform thickness but also defines the vertical adiabatic transitions to the Ti indiffused waveguides given by the circular shape of the blade.[24] A RIE post-thinning process has been developed to achieve a well-calibrated $LiNbO_3$ membrane thickness down to 500 nm without significantly affecting propagation losses. The manufactured rib waveguides have an 8 μm^2 targeted cross section with the following geometry: width = 3.83 μm, height = 1.23 μm, thickness = 800 nm, and sidewall angle = 16°.

B. Device characterization

Characterization of the linear optical properties of the component is first performed. Coupling losses with cleaved single-mode polarization maintaining (PM) fibers were estimated to be 0.8 dB, which is notably low compared to direct butt-coupling in a thin film lithium niobate (TFLN) waveguide. The overall propagation losses of the component, measured using the Fabry–Perot method,[25] are 0.39 ± 0.06 dB/cm for TM polarization and 1.09 ± 0.06 dB/cm for TE polarization. These values are higher than those observed in a reference component composed of a Ti-indiffused waveguide with a 2 μm thick membrane but without the rib waveguide, which exhibits propagation losses of 0.2 ± 0.06 dB/cm for both polarizations. The increased propagation loss is mainly attributed to the sidewall roughness of the rib waveguide as witnessed by the scanning electron microscope (SEM) image shown in Fig. 5. We estimated the losses in the 1 mm long nonlinear section to be 1.95 ± 0.2 and 0.61 ± 0.2 dB for TE and TM polarization, respectively. Improvement of the etching process or temperature annealing of the component should considerably reduce the propagation losses.[26]

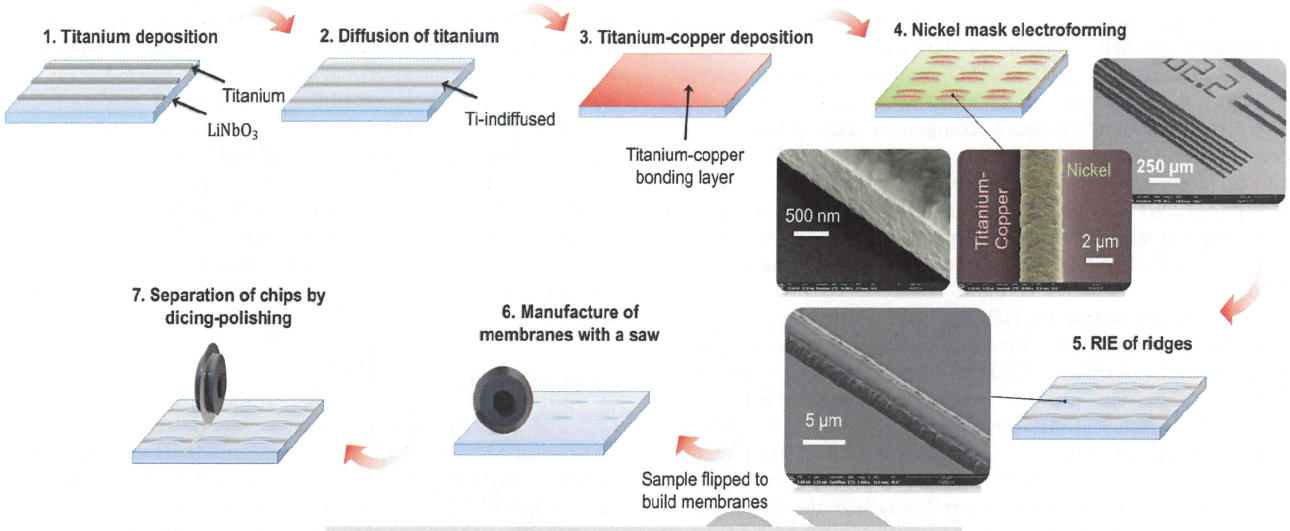

FIG. 5. Overview of the technological stages for the fabrication of the SHG device.

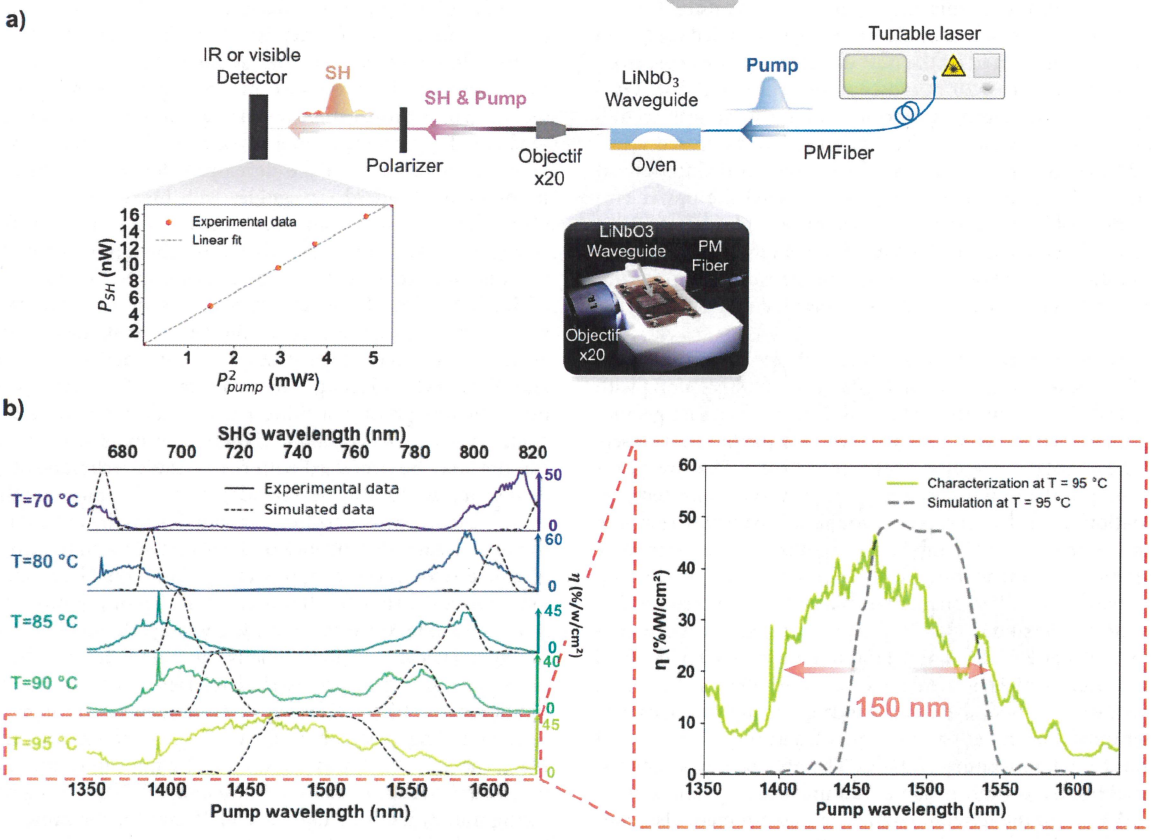

FIG. 6. (a) Schematic representation of the experimental setup to characterize the nonlinear component, including a plot that represents the evolution of the measured SH power with pump power at the pump wavelength of 1550 nm. (b) Measurements of the SHG conversion efficiency and comparison with numerical simulations.

The experimental setup schematically shown in Fig. 6(a) is used to measure the SHG response of the component. The sample is placed inside an oven (HCP OV30D), enabling temperature adjustments up to 200 °C with an accuracy of 0.1 °C. The pump beam is generated by using an optical component tester (CT440 EXFO) coupled with two tunable external-cavity lasers (T100S-HP ES and CL) for continuous wavelength scanning from 1350 to 1630 nm. The pump light excites the TM_{00} mode of the rib waveguide by butt-coupling via a PM fiber. The polarization at the fiber output has been accurately aligned with the crystal x axis using a rotating holder.

The output beams are collected with a microscope objective and detected with a silicon detector (Thorlabs S130C) and a germanium detector (Thorlabs S132C) for the second harmonic and pump beams, respectively. Figure 6(a) shows the relationship between the measured SH power at the waveguide output and the pump power at 1550 nm. In particular, an SH power of 17 nW was measured for a pump power of 2.3 mW. As expected from theory [Eq. (2)], the SH signal power increases quadratically with the pump power. Throughout the experiments, the waveguide exhibited no signs of damage, even at a maximum input pump power of 5 mW. The phase-matching response remained consistently stable and reproducible, independent of the pump power at this level. This stability was confirmed by three consecutive wavelength sweeps, each lasting 5 min. The conversion efficiency is then deduced using Eq. (2), where P_{pump} at the input of the nonlinear waveguide is deduced from the output pump measured by the NIR detector and corrected from four loss contributions: ×20 microscope objective (0.2 dB), Fresnel reflection (0.6 dB), propagation loss in the nonlinear section with the taper (0.61 dB), and in the 9 mm long Ti-indiffused waveguide (0.22 dB) giving a total loss of 1.63 dB. To deduce P_{SH} at the output of the nonlinear section, we corrected the power collected by the visible detector from an estimated total loss of 3 dB coming from the microscope objective, Fresnel reflection, propagation loss in the Ti-indiffused region, and in the rib waveguide with the taper transition, the latter being not optimized for the SH TE_{00} mode.

The measured SHG conversion efficiency spectra are shown in Fig. 6(b) for five temperatures ranging from 70 to 95 °C along with the numerical simulations that take into account the exact geometry of the manufactured component. The experimental data closely matched the simulation results shown in Fig. 6(b). The two peaks on either side of the pump telecom band converged with temperature variation until they merged, forming a broadband response of 150 nm centered on 1480 nm. These results pave the way for a new generation of compact frequency converters with a wide pump tunability bandwidth. The qualitative behavior agrees remarkably well with the predicted one. At 70 °C, two separated bands centered at pump wavelengths of 1350 and 1650 nm are frequency doubled with a maximum conversion efficiency close to 50%/(W/cm^2). As the temperature is raised, these two bands gradually shift closer to each other until they merge to give a broadband response centered at 1480 nm for a temperature of 95 °C. The obtained experimental phase-matching bandwidth is about 150 nm wide, spanning from 1400 to 1550 nm in the telecom band. The measurement also confirms that a tunability range as wide as 300 nm is achieved with a modest temperature variation of 25 °C. The main discrepancy between theory and experiment is the width of the different bands, which are wider experimentally. Two hypotheses can be given to explain this behavior. It could be due to a nonuniform cross section of the waveguide along propagation or to the tapered areas of the waveguide. It should be noted that the measured temperature tunability range, which is already fifteen times broader than the PPLN type-0 configuration,[27] is only limited by the tunability of our laser source. According to the simulations, an expected pump tunability range of 500 nm is achievable with this component by lowering its temperature to 20 °C. Moreover, simulations show that the tunability could be further extended to a range of 900 nm using a waveguide with a cross section of 23 μm^2 for a 200 °C temperature scan.

IV. DISCUSSION

The demonstrated nonlinear waveguide unveils key characteristics of SHG. The most appealing one is its giant continuous thermal tunability from 1.3 to 1.7 μm, which comprises the two main windows of the telecom wavelengths with a single component. In addition, a 150 nm phase-matching broadband centered near 1500 nm is available at a chosen temperature, which opens numerous possibilities for applications, such as femtosecond laser frequency doubling or other wavelength division multiplexing (WDM) applications. At last, by selecting the proper cross section of the waveguide, any pump wavelength from 1.05 to 3 μm can be frequency doubled, thus further extending the potential of the disclosed waveguide structure. It should be noted that a broadband conversion could also be envisioned in a waveguide with a varying cross section along propagation by analogy to Ref. 28, where a thermal gradient along propagation was used. Furthermore, the monolithic $LiNbO_3$ architecture of the developed device has salient features. It combines standard waveguides with highly confined regions to obtain record low coupling losses of 0.8 dB to $LiNbO_3$ film-based waveguides. We emphasize that this fabrication method offers a versatile way to realize, out of a single $LiNbO_3$ wafer, a variety of $LiNbO_3$ films from few microns down to submicron thickness. It can thus be seen as an alternative to standard LNOI films, avoiding the technological steps of ion implantation, bonding, annealing, and polishing. The nonlinear SHG waveguide based on birefringence phase matching has the advantage of a poling-free configuration. The required $LiNbO_3$ layer thickness, around 2 μm, can not only be produced with the versatile technique of precision dicing but could also be extended to the bonding-polishing process.[29] A few centimeters long waveguides are then possible. Thanks to the quadratic dependence of the SH power with the length, overall conversion efficiency approaching 100% could be reached in cms long devices with a few hundred of mW pump power. This solution is feasible since the unveiled waveguide architecture relaxes the geometrical tolerances relative to the phase-matching conditions. The stringent geometrical tolerance is indeed a significant limitation for PPLNOI waveguides or requires complex solutions such as poling post-correction to adapt to thickness variations.[30] For instance, a thickness variation of 2.2 nm can result in a 50-fold decrease in SH emission for a 5 mm long PPLNOI waveguide.[31] Our configuration allows a tolerance of 10 nm for the same waveguide length, which relaxes 5 times the tolerance manufacturing, which opens the possibility to benefit from improved global conversion efficiency.

V. CONCLUSION

To conclude, the unveiled SHG component opens new perspectives for implementing versatile and low-cost wide-band spectral applications. In particular, the record temperature tunability range and the broadband response at telecom wavelengths have foreseen significant advancements for WDM communications. At last, the tunable and flat dispersion properties of the waveguide could also be exploited for other configurations, such as sum and difference frequency generation to further extend its interest.

ACKNOWLEDGMENTS

This work has been partially funded by the SYRAH-lab project (Contract No. "ANR-19- LCV2-0007-01") and the NanoFiLN project (Grant No. ANR-23-PEEL-0004), supported by the EIPHI Graduate school (Contract No. ANR-17-EURE-0002") and the French RENATECH network through its FEMTO-ST technological facility.

AUTHOR DECLARATIONS

Conflict of Interest

The authors have no conflicts to disclose.

Author Contributions

Aiman Zinaoui: Conceptualization (equal); Data curation (equal); Formal analysis (equal); Investigation (equal); Methodology (equal); Validation (equal); Writing – original draft (equal); Writing – review & editing (equal). **Lucas Grosjean**: Conceptualization (equal); Formal analysis (equal); Investigation (equal); Methodology (equal); Visualization (equal). **Arthur De Sousa Lopes Moreira**: Formal analysis (equal); Investigation (equal); Resources (equal). **Miguel Angel Suarez**: Conceptualization (equal); Data curation (equal); Formal analysis (equal); Investigation (equal); Methodology (equal); Resources (equal); Validation (equal); Visualization (equal); Writing – review & editing (equal). **Samuel Queste**: Conceptualization (equal); Formal analysis (equal); Investigation (equal); Methodology (equal); Resources (equal); Validation (equal); Visualization (equal). **Laurent Robert**: Conceptualization (equal); Formal analysis (equal); Investigation (equal); Methodology (equal); Resources (equal); Validation (equal); Visualization (equal). **Ludovic Gauthier-Manuel**: Conceptualization (equal); Formal analysis (equal); Investigation (equal); Methodology (equal); Resources (equal); Validation (equal); Visualization (equal). **Mathieu Chauvet**: Conceptualization (equal); Data curation (equal); Formal analysis (equal); Funding acquisition (equal); Investigation (equal); Methodology (equal); Project administration (equal); Resources (equal); Supervision (equal); Validation (equal); Visualization (equal); Writing – original draft (equal); Writing – review & editing (equal). **Nadège Courjal**: Conceptualization (equal); Data curation (equal); Formal analysis (equal); Funding acquisition (equal); Investigation (equal); Methodology (equal); Project administration (equal); Resources (equal); Supervision (equal); Validation (equal); Visualization (equal); Writing – original draft (equal); Writing – review & editing (equal).

DATA AVAILABILITY

The data that support the findings of this study are available from the corresponding author upon reasonable request.

REFERENCES

[1]T. Inagaki, K. Inaba, T. Leleu, T. Honjo, T. Ikuta, K. Enbutsu, T. Umeki, R. Kasahara, K. Aihara, and H. Takesue, "Collective and synchronous dynamics of photonic spiking neurons," Nat. Commun. **12**, 2325 (2021).

[2]A. Y. Hwang, H. S. Stokowski, T. Park, M. Jankowski, T. P. McKenna, C. Langrock, J. Mishra, V. Ansari, M. M. Fejer, and A. H. Safavi-Naeini, "Mid-infrared spectroscopy with a broadly tunable thin-film lithium niobate optical parametric oscillator," Optica **10**, 1535 (2023).

[3]Z. Ma, J.-Y. Chen, Z. Li, C. Tang, Y. M. Sua, H. Fan, and Y.-P. Huang, "Ultrabright quantum photon sources on chip," Phys. Rev. Lett. **125**, 263602 (2020).

[4]X. Wang, X. Jiao, B. Wang, Y. Liu, X.-P. Xie, M.-Y. Zheng, Q. Zhang, and J.-W. Pan, "Quantum frequency conversion and single-photon detection with lithium niobate nanophotonic chips," npj Quantum Inf. **9**, 38 (2023).

[5]C. Wang, C. Langrock, A. Marandi, M. Jankowski, M. Zhang, B. Desiatov, M. M. Fejer, and M. Lončar, "Ultrahigh-efficiency wavelength conversion in nanophotonic periodically poled lithium niobate waveguides," Optica **5**, 1438 (2018).

[6]D. N. Nikogosian, *Nonlinear Optical Crystals: A Complete Survey* (Springer-Science, New York, 2005).

[7]E. Hwang, N. Harper, R. Sekine, L. Ledezma, A. Marandi, and S. Cushing, "Tunable and efficient ultraviolet generation with periodically poled lithium niobate," Opt. Lett. **48**, 3917 (2023).

[8]B. Desiatov, A. Shams-Ansari, M. Zhang, C. Wang, and M. Lončar, "Ultra-low-loss integrated visible photonics using thin-film lithium niobate," Optica **6**, 380 (2019).

[9]K.-D. F. Büchter, H. Herrmann, C. Langrock, M. M. Fejer, and W. Sohler, "All-optical Ti:PPLN wavelength conversion modules for free-space optical transmission links in the mid-infrared," Opt. Lett. **34**, 470 (2009).

[10]X. Wu, L. Zhang, Z. Hao, R. Zhang, R. Ma, F. Bo, G. Zhang, and J. Xu, "Broadband second-harmonic generation in step-chirped periodically poled lithium niobate waveguides," Opt. Lett. **47**, 1574 (2022).

[11]M. Jankowski, J. Mishra, and M. M. Fejer, "Dispersion-engineered $\chi^{(2)}$ nanophotonics: A flexible tool for nonclassical light," J. Phys. Photonics **3**, 042005 (2021).

[12]M. Jankowski, C. Langrock, B. Desiatov, A. Marandi, C. Wang, M. Zhang, C. R. Phillips, M. Lončar, and M. M. Fejer, "Ultrabroadband nonlinear optics in nanophotonic periodically poled lithium niobate waveguides," Optica **7**, 40 (2020).

[13]J. Zhao, X. Li, T.-C. Hu, A. A. Sayem, H. Li, A. Tate, K. Kim, R. Kopf, P. Sanjari, M. Earnshaw, N. K. Fontaine, C. Wang, and A. Blanco-Redondo, "Unveiling the origins of quasi-phase matching spectral imperfections in thin-film lithium niobate frequency doublers," APL Photonics **8**, 126106 (2023).

[14]Y. Zhang, H. Li, T. Ding, Y. Huang, L. Liang, X. Sun, Y. Tang, J. Wang, S. Liu, Y. Zheng, and X. Chen, "Scalable, fiber-compatible lithium-niobate-on-insulator micro-waveguides for efficient nonlinear photonics," Optica **10**, 688 (2023).

[15]J. J. Chakkoria, R. A. Aoni, A. Dubey, G. Ren, T. G. Nguyen, A. Boes, S. K. Selvaraja, and A. Mitchell, "Efficient poling-free wavelength conversion in thin film lithium niobate harnessing bound states in the continuum," Laser Photonics Rev. ■, 2301335 (2024).

[16]X. Shi, S. S. Mohanraj, V. Dhyani, A. A. Baiju, S. Wang, J. Sun, L. Zhou, A. Paterova, V. Leong, and D. Zhu, "Efficient photon-pair generation in layer-poled lithium niobate nanophotonic waveguides," Light: Sci. Appl. **13**, 282 (2024); arXiv:2405.10943 [physics.optics].

[17]T. Ding, Y. Tang, H. Li, S. Liu, J. Zhang, Y. Zheng, and X. Chen, "Noncritical birefringence phase-matched second harmonic generation in a lithium-niobate-on-insulator micro-waveguide for green light emission," Opt. Lett. **49**, 1121 (2024).

[18]R. Luo, Y. He, H. Liang, M. Li, and Q. Lin, "Highly tunable efficient second-harmonic generation in a lithium niobate nanophotonic waveguide," Optica **5**, 1006 (2018).
[19]M. Mwangi, F. Behague, A. Coste, J. Safioui, M. Suarez, J. Byiringiro, P. Lutz, C. Clévy, and N. Courjal, "In-situ phase control of a low-loss membrane-based lithium-niobate polarisation-state modulator," Opt. Continuum **1**, 2513 (2022).
[20]D. E. Zelmon, D. L. Small, and D. Jundt, "Infrared corrected Sellmeier coefficients for congruently grown lithium niobate and 5 mol. % magnesium oxide–doped lithium niobate," J. Opt. Soc. Am. B **14**, 3319 (1997).
[21]D. H. Jundt, "Temperature-dependent Sellmeier equation for the index of refraction, n_e, in congruent lithium niobate," Opt. Lett. **22**, 1553 (1997).
[22]U. Schlarb and K. Betzler, "Refractive indices of lithium niobate as a function of temperature, wavelength, and composition: A generalized fit," Phys. Rev. B **48**, 15613–15620 (1993).
[23]C. Lu, Y. Zhang, J. Qiu, Y. Tang, T. Ding, S. Liu, Y. Zheng, and X. Chen, "Highly tunable birefringent phase-matched second-harmonic generation in an angle-cut lithium niobate-on-insulator ridge waveguide," Opt. Lett. **47**, 1081 (2022).
[24]N. Courjal, A. Caspar, V. Calero, G. Ulliac, M. Suarez, C. Guyot, and M.-P. Bernal, "Simple production of membrane-based $LiNbO_3$ micro-modulators with integrated tapers," Opt. Lett. **41**, 5110 (2016).
[25]A. Gerthoffer, C. Guyot, W. Qiu, A. Ndao, M.-P. Bernal, and N. Courjal, "Strong reduction of propagation losses in $LiNbO_3$ ridge waveguides," Opt. Mater. **38**, 37–41 (2014).
[26]A. Shams-Ansari, G. Huang, L. He, Z. Li, J. Holzgrafe, M. Jankowski, M. Churaev, P. Kharel, R. Cheng, D. Zhu, N. Sinclair, B. Desiatov, M. Zhang, T. J. Kippenberg, and M. Lončar, "Reduced material loss in thin-film lithium niobate waveguides," APL Photonics **7**, 081301 (2022).
[27]M. Fejer, G. Magel, D. Jundt, and R. Byer, "Quasi-phase-matched second harmonic generation: Tuning and tolerances," IEEE J. Quantum Electron. **28**, 2631–2654 (1992).
[28]Y. Tang, T. Ding, C. Lu, J. Qiu, Y. Zhang, Y. Huang, S. Liu, Y. Zheng, and X. Chen, "Broadband second-harmonic generation in an angle-cut lithium niobate-on-insulator waveguide by a temperature gradient," Opt. Lett. **48**, 1108 (2023).
[29]V. Pecheur, H. Porte, J. Hauden, F. Bassignot, M. Deroh, and M. Chauvet, "Watt-level SHG in undoped high step-index PPLN ridge waveguides," OSA Continuum **4**, 1404–1414 (2021).
[30]P.-K. Chen, I. Briggs, C. Cui, L. Zhang, M. Shah, and L. Fan, "Adapted poling to break the nonlinear efficiency limit in nanophotonic lithium niobate waveguides," Nat. Nanotechnol. **19**, 44–50 (2024).
[31]P. S. Kuo, "Noncritical phasematching behavior in thin-film lithium niobate frequency converters," Opt. Lett. **47**, 54 (2022).